SPECIAL
Air-sea interaction during PISTON-MISOBOB-CAMP2Ex
COLLECTION

On Characterizing Ocean Kinematics from Surface Drifters

SEBASTIAN ESSINK,[a] VERENA HORMANN,[b] LUCA R. CENTURIONI,[b] AND AMALA MAHADEVAN[c]

[a] *Applied Physics Laboratory, University of Washington, Seattle, Washington*
[b] *Lagrangian Drifter Laboratory, Scripps Institution of Oceanography, University of California, San Diego, La Jolla, California*
[c] *Woods Hole Oceanographic Institution, Woods Hole, Massachusetts*

(Manuscript received 1 June 2021, in final form 20 April 2022)

ABSTRACT: Horizontal kinematic properties, such as vorticity, divergence, and lateral strain rate, are estimated from drifter clusters using three approaches. At submesoscale horizontal length scales $\mathcal{O}(1–10)$ km, kinematic properties become as large as planetary vorticity f, but challenging to observe because they evolve on short time scales $\mathcal{O}$(hours to days). By simulating surface drifters in a model flow field, we quantify the sources of uncertainty in the kinematic property calculations due to the deformation of cluster shape. Uncertainties arise primarily due to (i) violation of the linear estimation methods and (ii) aliasing of unresolved scales. Systematic uncertainties (iii) due to GPS errors, are secondary but can become as large as (i) and (ii) when aspect ratios are small. Ideal cluster parameters (number of drifters, length scale, and aspect ratio) are determined and error functions estimated empirically and theoretically. The most robust method—a two-dimensional, linear least squares fit—is applied to the first few days of a drifter dataset from the Bay of Bengal. Application of the length scale and aspect-ratio criteria minimizes errors (i) and (ii), and reduces the total number of clusters and so computational cost. The drifter-estimated kinematic properties map out a cyclonic mesoscale eddy with a surface, submesoscale fronts at its perimeter. Our analyses suggest methodological guidance for computing the two-dimensional kinematic properties in submesoscale flows, given the recently increasing quantity and quality of drifter observations, while also highlighting challenges and limitations.

SIGNIFICANCE STATEMENT: The purpose of this study is to provide insights and guidance for computing horizontal velocity gradients from clusters (i.e., three or more) of Lagrangian surface ocean drifters. The uncertainty in velocity gradient estimates depends strongly on the shape deformation of drifter clusters by the ocean currents. We propose criteria for drifter cluster length scales and aspect ratios to reduce uncertainties and develop ways of estimating the magnitude of the resulting errors. The findings are applied to a real ocean dataset from the Bay of Bengal.

KEYWORDS: Indian Ocean; Eddies; Frontogenesis/frontolysis; Fronts; Lagrangian circulation/transport; Ocean circulation; Ocean dynamics

1. Introduction

Measuring kinematic properties is of particular interest at submesoscales (0.1–10 km length scales), where lateral buoyancy gradients are intensified by surface forcing, topographic interaction, frontogenesis, baroclinic instability, and turbulent thermal wind. Large local Rossby number $\mathrm{Ro} = \zeta/f \sim \mathcal{O}(1)$ can be generated, where $\zeta = v_x - u_y$ is the relative vorticity and f is the Coriolis frequency (e.g., Thomas et al. 2008; McWilliams 2016), along with other kinematic properties. It has been established from both theory (e.g., Rudnick 2001) and modeling (e.g., Mahadevan and Tandon 2006; Ramachandran et al. 2018) that energetic submesoscale turbulence develops positively skewed relative vorticity of $\mathcal{O}(f)$, lateral strain rate of $\mathcal{O}(f)$, and horizontal convergence that leads to vertical velocities of $\mathcal{O}(100)$ m day^{-1} (e.g., Shcherbina et al. 2013; Ruiz et al. 2019).

In the past decade, a growing number of experiments (e.g., Poje et al. 2014; Berta et al. 2016; Tarry et al. 2021) have deployed large numbers of drifters to measure dispersion characteristics of submesoscale flows and their kinematic properties. Kinematic properties can be derived from sets of at least three synchronous velocity measurements in space. Three methods that have historically been applied to drifter datasets are the focus of this study: Saucier (1955) derived divergence from three wind measurements in the atmosphere assuming that the area spanned by the weather stations must be conserved (e.g., Niiler et al. 1989; Fahrbach et al. 1986). Kawai (1985a,b) used Stokes's and Gauss's theorems to compute area-averaged vorticity and divergence by taking the line integral of velocity around the circumference of a polygon of drifters. Müller et al. (1988) and Lien and Müller (1992) used a similar approach on triangles of acoustic Doppler current profiler (ADCP) measurements to compute vorticity and divergence at different depths. Molinari and Kirwan (1975) and Okubo and Ebbesmeyer (1976) fitted horizontal drifter velocities with a bilinear function to yield the velocity gradients. As the number of drifters exceeds three, this method minimizes the error of the fit in a least squares (LS) sense and provides an estimate of uncertainty—both of which are reasons why this method is most

Corresponding author: Sebastian Essink, sessink@uw.edu

DOI: 10.1175/JTECH-D-21-0068.1

broadly used (e.g., Fahrbach et al. 1986; Paduan and Niiler 1990; Swenson et al. 1992; Righi and Strub 2001; Tarry et al. 2021). More recently, Oscroft et al. (2020) extended the LS method to also fit parameters in time to a slowly varying mesoscale velocity and derived a velocity decomposition into mesoscale and submesoscale contributions. The challenge is that, since true velocity fields are unknown (particularly at small scales), kinematic property errors are difficult to estimate. The choice of method is also motivated by usability and computational cost, so that large numbers of drifter trajectories can be analyzed.

The goal of this study is to estimate kinematic properties from clusters of drifters. First, we evaluate the performance of the above three methods by estimating the kinematic properties using synthetic drifters in a numerical model and compute error estimates. Then, we apply the criteria and guidance to a real ocean dataset from the Bay of Bengal.

However, measuring spatial derivatives of velocity is challenging in the ocean because it requires simultaneous measurements in space. Shipboard velocity measurements only capture variability in the along-track direction, therefore, missing one component of the two-dimensional gradient (e.g., Callies and Ferrari 2013). Shcherbina et al. (2013) found vertical vorticity and strain rate exceeding $\mathcal{O}(f)$ in the near-surface ocean using one of the first two-ship surveys. High-frequency (HF) and X-band radar systems (e.g., Kirincich et al. 2013; Horstmann et al. 2015; Lund et al. 2012) are able to capture velocity fields at subkilometer horizontal and subhourly temporal resolution. In coastal regions, for example, these were used to map statistics of kinematic properties of submesoscale eddies (Kirincich 2016). Aerial imagery taken from planes and drones are promising to resolve submesoscale variability and infer currents at a high spatial resolution (e.g., Marmorino et al. 2018, 2010; Karimova and Gade 2016).

Discrete spatial measurements of velocity will likely generate uncertainty in the velocity gradient estimates, regardless of the measurement platform and method. This is largely due to the variability of kinematic properties at unresolved scales, which causes significant aliasing (e.g., Lien and Müller 1992; Müller et al. 1988). Wavenumber spectra at scales below ~10 km in the ocean are underobserved and limited by horizontal resolution of the measurement platforms. In addition, Kunze et al. (1990) found using ADCP measurements that discrete velocity measurements in space make it difficult to differentiate between divergence and vorticity. For example, when using Stokes's theorem to compute vorticity on the perimeter of discrete velocity measurements, divergence at scales below the separation scale of individual measurements can contaminate the vorticity estimate, and vice versa.

Previous studies using drifter-based methods reported several operational challenges (e.g., Kirwan 1988) because drifter clusters are advected by the flow and deform. Kinematic properties in regions of the strongest velocity gradients are the most challenging to capture and often only observable for a short period of time until the drifter clusters become too deformed. Since the kinematic properties are a function of scale, the signal-to-noise ratio strongly depends on the length scale of the drifter clusters (e.g., Righi and Strub 2001; Paduan and Niiler 1990; Ohlmann et al. 2017; Berta et al. 2016). Hormann et al. (2016) were able to compute mesoscale vorticity with the Saucier method from the same dataset used in this study but retrieved ambiguous noisy estimates at scales $L < 10$ km. Ohlmann et al. (2017) and Righi and Strub (2001) further noted that elongated and deformed clusters induce larger errors of the kinematic properties. Spydell et al. (2019) used stationary global positioning system (GPS) beacons and the LS method to estimate the error of vorticity purely due to the GPS error. Tarry et al. (2021) found the GPS vorticity error to be as large as the submesoscale signal, even for fast-reporting GPS beacons. Alignment of drifters in the direction of fronts biases the sampling toward regions of larger shear and convergence (e.g., Pearson et al. 2019), and is unfavorable when trying to estimate cross-frontal gradients.

A nonhydrostatic Boussinesq model is spun up from a strong lateral buoyancy gradient (Mahadevan et al. 1996a,b). Synthetic drifter clusters are introduced in the model's surface flow to sample the velocity field. Cluster characteristics, such as the number of drifters per cluster N, the aspect ratio α, and the cluster length scale L, are varied systematically to investigate the error in the kinematic-property estimation for each of the three methods. This idealized sensitivity study helps to constrain the sources of error, and ascertain the parameter dependence on N, L, and α, which can be evaluated when working with observational drifter data, and aid in the interpretation of the kinematic property results. Errors due to GPS uncertainties and cluster shape deformation are also estimated with the same set of parameters (i.e., N, L, and α).

Using the insights from the numerical model, we apply the LS method to a large, high-resolution near-surface drifter dataset collected in the Bay of Bengal as part of the Air–Sea Interactions Regional Initiative (ASIRI) (Wijesekera et al. 2016; Lucas et al. 2014; Hormann et al. 2016; Essink et al. 2019)—a predecessor of the ongoing program, Monsoon Intraseasonal Oscillations in the Bay of Bengal (MISO-BOB) (Shroyer et al. 2021). ASIRI's primary goal has been to study processes in the upper ocean to better understand their role for air–sea fluxes and the monsoon (Lucas et al. 2014; Wijesekera et al. 2016). In 2015, drifters were deployed across a freshwater-dominated density front with the goal of better understanding the processes that disperse the freshwater (Essink et al. 2019; Hormann et al. 2016) originating from major rivers in the northern bay and intense precipitation during the monsoon (Mahadevan et al. 2016).

This study is organized as follows. In section 2, the drifter dataset, the numerical model, and the methods for estimating the velocity gradients are described. In section 3, the methods are tested in the numerical model and the sensitivity to the geometry of drifter clusters is determined using a known velocity field. Error functions due to shape deformation and GPS error are estimated. In section 4, we describe how the observed drifter clusters deform, present time series and maps of the estimated kinematic properties and relate them to the observed ocean physics. A summary and conclusions are provided in section 5.

2. Data and methods

a. *Bay of Bengal drifter dataset*

A total of 46 drifters (one of which failed upon deployment) were released in the northern Bay of Bengal, at the edge of a

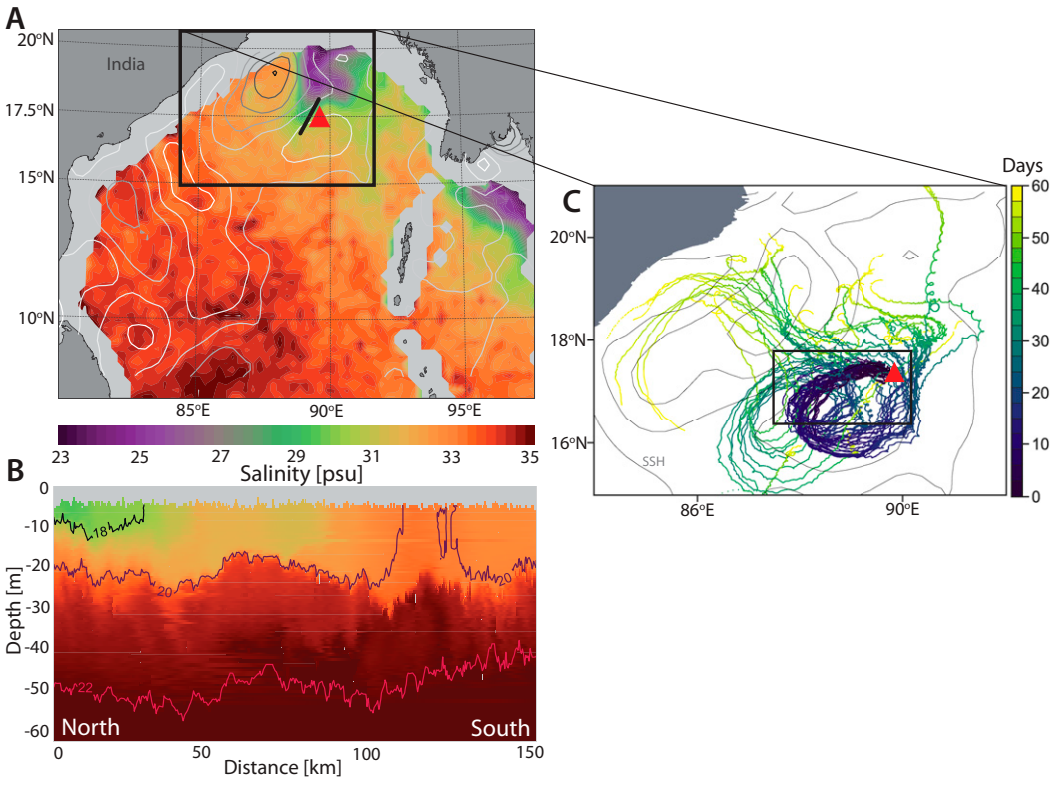

FIG. 1. (a) Map of the Bay of Bengal on 23 Aug 2015, one week before the drifter deployments. Sea surface salinity from the Soil Moisture Active Passive (SMAP) mission is shown in color (Entekhabi et al. 2010). Light (dark) contours are positive (negative) sea level anomalies from delayed-time, gridded 0.25° Copernicus Marine Environment Monitoring Service (CMEMS) data (Traon et al. 1998; Ducet et al. 2000). The drifter release location is marked by the red triangle. (b) Example north–south CTD section of salinity with density contours collected on 15 Sep 2015 along a section shown as a thick black line in (a). (c) Two months of drifter trajectories released at the red triangle overlaid onto CMEMS sea level anomalies with days after deployment are shown in color.

strong cyclonic eddy and across a freshwater-dominated density front (Hormann et al. 2016; Essink et al. 2019) (Fig. 1). Surface Velocity Program (SVP) drifters drogued at 15-m depth minimize Stokes drift by surface gravity waves and wind slippage (Niiler et al. 1995; Centurioni 2018). Since mixed layers were shallow (see Fig. 1b), this drogue depth might affect the extent to which mixed layer currents are sampled. All drifters were equipped with a thermistor centimeters below the surface. Thirty-six drifters carried an additional conductivity sensor at about 0.5-m depth to infer salinity (Hormann et al. 2015, 2016) and allowing to compute near-surface density which is largely controlled by changes in salinity in the Bay of Bengal (e.g., Jaeger and Mahadevan 2018; Mahadevan et al. 2016).

The drifters were programmed to report GPS positions at 5-min intervals during the first month of deployment and at 30-min intervals thereafter, sufficient to resolve submesoscale variability. To resolve flow patterns at length scales from 1 to 30 km, the drifters were released in tight clusters of four drifters with $\mathcal{O}(1)$ km initial separation. Ten clusters formed a larger swarm spanning an area of about 30 km^2 (Hormann et al. 2016). The following analysis is an expansion of the work in Hormann et al. (2016), where this dataset was used to provide first estimates of the kinematic properties using the Saucier method.

b. Numerical model

The nonhydrostatic Process Study Ocean Model (PSOM) (Mahadevan et al. 1996a,b) was used to simulate a submesoscale flow field, initialized with a strong density front measured in the northern Bay of Bengal in 2013 with a profiling conductivity–temperature–depth (CTD) probe. The model initial condition is characterized by a north–south buoyancy gradient set up by riverine freshwater in the northern bay, similar to conditions during the 2015 field campaign (Jaeger and Mahadevan 2018) during which the drifter data were collected.

The model is in channel configuration, periodic in east–west and with solid boundaries in the north–south direction, spanning a 320 × 190 km^2 area with a 1000-m flat bottom. The horizontal grid resolution is $\Delta x = \Delta y = 1$ km, sufficient to resolve submesoscale variability. The vertical coordinate is exponentially stretched over 35 levels with $\Delta z \approx 2$ m at the surface and $\Delta z \approx 100$ m at the bottom. The simulation is stepped forward with a time step of $\Delta t \approx 5$ min. A constant-

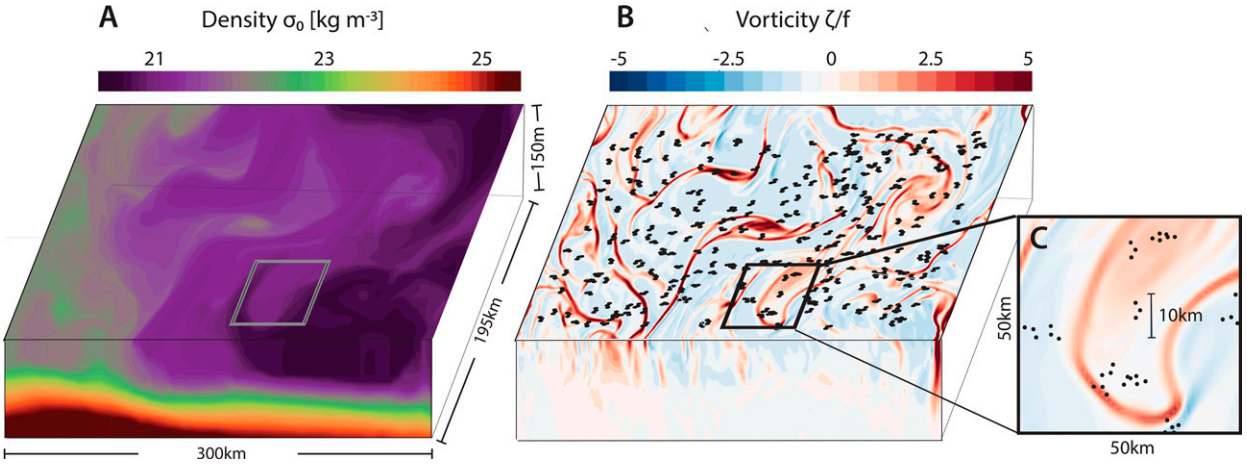

FIG. 2. Three-dimensional image of the fully spun-up numerical simulation. Front and top faces of the domain are shown of (a) density anomaly, $\sigma_0 = \rho - 1000$ kg m^{-3}, showing a ~50-m mixed layer and strong cross-domain density gradients and (b) relative vorticity ζ normalized by the Coriolis frequency f showing strong filaments and eddies that reach vorticity magnitudes of up to 5f. Overlaid black dots are examples of drifter clusters at random positions. (c) Zoom onto a filament with drifter clusters, each made up of three drifters.

diffusivity along-isopycnal mixing is used with $\kappa \approx 1$ m^2 s^{-1} (Redi 1982) and a "K profile parameterization" (KPP) for vertical mixing (Large et al. 1994).

The simulation is forced with realistic wind stress and heat fluxes measured by a mooring at 18°N in the Bay of Bengal (Weller et al. 2016). The surface forcing counteracts a loss of eddy kinetic energy. During initialization, the north–south front becomes unstable to shear and baroclinic instability and breaks up into smaller eddies with diameters of $\mathcal{O}(1–10)$ km. After about 30 days, the domain-averaged kinetic energy changes slowly, mean mixed layer depth stabilizes at ~50 m, and a fully eddying flow field emerges.

Examples of the spun-up density and vorticity fields are shown in Fig. 2. Stirring by eddies generates elongated filaments of sharp density gradient with vorticity of up to 5f. The distribution of vorticity is positively skewed; that is, larger positive flow features being more frequent than negative eddies. Furthermore, positive-vorticity filaments and fronts are associated with strong downward velocity in their vicinity (not shown).

The model is a process study model with limited spatial domain. We do not claim that it models the Bay of Bengal accurately because it is missing the large-scale circulation context, topography, and large-scale atmospheric forcing that other regional models would include. All of these can change the nature and length scale of fronts. In the model, the smallest scales (or the sharpest fronts) are set by the resolved physics that provide frontogenetic tendencies and the resolved and unresolved processes that mix to dissipate fronts. Our model only parameterizes subgrid-scale mixing, so the frontal scale is close to the grid scale (like it is the case in many models).

c. Estimation of kinematic properties

The two-dimensional velocity gradient tensor $G_{ij} = \partial u_i/\partial x_j$ of the horizontal velocity u_i can be written as the sum of symmetric and antisymmetric parts, $G^{\text{sym}} = (G_{ij} + G_{ji})/2$, and $G^{\text{anti}} = (G_{ij} - G_{ji})/2$. The antisymmetric part describes the rotations of a fluid parcel. Its two nonzero components are $\pm\zeta/2$, where ζ is the vertical component of the relative vorticity. The trace of the symmetric part is the horizontal divergence $\delta = G_{ii}^{\text{sym}}$ and its off-diagonal components $G_{i\neq j}^{\text{sym}}$ are the shear and normal strain rates. The eigenvalues of G are the rates at which two particles separate, subject to the divergence, strain, and shear of the flow. The sum of the eigenvalues is equal to the divergence δ. Vorticity, horizontal divergence, shear, and normal strain rates are defined as $\zeta \equiv v_x - u_y$, $\delta \equiv u_x + v_y$, $S_s \equiv v_x + u_y$, and $S_n \equiv u_x - v_y$, respectively. Lateral strain rate is defined as $S \equiv \sqrt{S_s^2 + S_n^2}$.

We focus on the three methods that have previously been applied to drifter observations: (i) the Saucier method based on the area rate of change of a drifter cluster first documented by Saucier (1953, 1955), (ii) the Kawai method (e.g., Kawai 1985a,b) based on Stokes's and Gauss's theorems, and (iii) the LS method (e.g., Molinari and Kirwan 1975). All of these methods require at least three measurements (i.e., $N \geq 3$) of velocity and position in space.

The Saucier method (Saucier 1953, 1955), first applied to wind measurements at three weather stations separated by $\mathcal{O}(100)$ km, assumes that properties between the stations are conserved. Divergence can then be derived by evaluating the rate of change of the area A spanned by the stations:

$$\overline{\delta} = \frac{1}{A(t)} \frac{A(t + \Delta t) - A(t)}{\Delta t}, \tag{1}$$

where t is time and Δt set by the sampling period. By rotating the coordinate system, Saucier (1953) transformed the expression for vorticity into an expression for the divergence of the rotated velocity (u', v'), $\zeta = v_x - u_y \rightarrow u'_x + v'_y = (1/A')\{[A'(t + \Delta t) - A'(t)]/\Delta t\}$, which can be evaluated like above. Analogously, normal and shear strain rates can be computed by applying a different rotation.

Kawai (1985a) used Stokes's and Gauss's theorems to estimate divergence and vorticity by evaluating path integrals around the area spanned by a drifter cluster:

$$\overline{\delta} = \frac{1}{A}\oint\!\!\int \delta dA = \frac{1}{A}\oint\!\!\int (\mathbf{u}\cdot d\mathbf{n}), \tag{2}$$

$$\overline{\zeta} = \frac{1}{A}\oint\!\!\int \zeta dA = \frac{1}{A}\oint\!\!\int (\mathbf{u}\cdot d\mathbf{t}), \tag{3}$$

where overbars are averages over the cluster-spanned area, tangential (**t**) and normal (**n**) unit vectors relative to the perimeter of A. In practice, the drifter velocities are interpolated onto the polygon edges; that is, the midpoints between drifter positions. The number of drifters involved and the distance they are apart are important for how well the true path integral can be computed with discrete measurements.

Molinari and Kirwan (1975) and Okubo and Ebbesmeyer (1976) developed a bilinear fit to the drifter velocities to determine the velocity gradients. At each instant in time, six parameters are fitted: two mean-flow components $(\overline{u}, \overline{v})$ and four two-dimensional velocity gradient components. At least three points (i.e., $N \geq 3$) for each velocity component are needed to solve this system.

The method can be derived from a Taylor expansion of each drifter's velocity (u_i, v_i) about the center of mass $(\overline{x}, \overline{y})$ of a drifter cluster, which gives the following system of equations:

$$u_i = \overline{u} + \frac{\partial u}{\partial x}(x_i - \overline{x}) + \frac{\partial u}{\partial y}(y_i - \overline{y}) + \mathcal{O}(\Delta x^2), \tag{4}$$

$$v_i = \overline{v} + \frac{\partial v}{\partial x}(x_i - \overline{x}) + \frac{\partial v}{\partial y}(y_i - \overline{y}) + \mathcal{O}(\Delta x^2), \tag{5}$$

where (x_i, y_i) is each drifter's position. The expansion is truncated at the first order, with the error scaling like $\mathcal{O}(\Delta x^2)$, making this a linear method. The linear method implies that parameters are homogeneous across the length scale of a drifter cluster. The residual represents higher-order terms and can be attributed to turbulent motions as described in Molinari and Kirwan (1975).

We rewrite Eq. (4) in matrix form, using $\mathbf{C}_u = (\overline{u}, \partial u/\partial x, \partial u/\partial y)$, $\mathbf{C}_v = (\overline{v}, \partial v/\partial x, \partial v/\partial y)$ and distance matrix $\mathbf{Q} = (1, x_i - \overline{x}, y_i - \overline{y})$ which contains the distances in x and y relative to the cluster center of mass. The terms $\mathbf{U}'$ and $\mathbf{V}'$ now contain the $\mathcal{O}(\Delta x^2)$ terms representing turbulence at scales smaller than the polygon scale:

$$\mathbf{U} = \mathbf{Q}\mathbf{C}_u + \mathbf{U}', \tag{6}$$

$$\mathbf{V} = \mathbf{Q}\mathbf{C}_v + \mathbf{V}'. \tag{7}$$

To solve (6) and (7), we assumed that $\mathbf{U}'$ and $\mathbf{V}'$ are negligible at small separations Δx and Δy. The values of $\mathbf{C}_u$ and $\mathbf{C}_v$ can be found by minimizing the sum of squares $\|\mathbf{Q}\mathbf{C}_u - \mathbf{Q}\|^2$ and $\|\mathbf{Q}\mathbf{C}_v - \mathbf{V}\|^2$.

The coefficient vectors of the bilinear fit, $\mathbf{C}_u$ and $\mathbf{C}_v$, contain the mean-flow components and spatial derivatives of the horizontal velocity. These can be combined into the vertical component of the vorticity ζ, the divergence δ, and the lateral strain rate S.

3. Model-based evaluation of methods

We use the three methods above to compute the kinematic properties of the model velocity field, compare their accuracy, and identify the uncertainties associated with sparse spatial data and the geometry of drifter clusters. We also compute theoretical and empirical error functions.

a. Comparison of methods

The kinematic properties are calculated for synthetic drifter clusters, each of which can be described by the number of drifters N, the cluster length scale L, and its aspect ratio α as defined below. For each set of parameters, a total of 10 000 clusters of synthetic drifters are seeded in the model domain (Fig. 2a) at random locations and with random orientations.

Note that the synthetic drifters are not advected by the flow, so that natural deformation of drifter clusters by convergences or shear flows is eliminated entirely and drifters do not sample the flow in a biased way like actual drifters would (e.g., Pearson et al. 2019). Instead, synthetic drifters only sample the model's velocity field with a cubic spline interpolation at the drifters' position. The parameter space of cluster shapes will be explored systematically by choosing N, L, and α.

We define the length scale of a drifter cluster as the root-mean-square (rms) distance between all pairs of drifters $L \equiv \sqrt{\langle (x_i - x_j)^2 \rangle}$, where the angle brackets indicate the mean over all pairs in a cluster; L is normalized by the flow length scale L_u, which is determined from the horizontal wavenumber spectra of velocity and velocity gradients (Fig. 3). We expect L_u to be a fair representation for both velocity components because the grid is regular in both horizontal directions. In the model simulation the flow length scale is $L_u \approx 5$ km.

The aspect ratio $\alpha = \lambda_{\min}/\lambda_{\max}$ is defined as the ratio of minor and major eigenvalues $\lambda_{\min}/\lambda_{\max}$ of the position covariance matrix $\mathrm{cov}(\mathbf{X}, \mathbf{X}^{\mathrm{T}})$, where $\mathbf{X}$ is the matrix of positions (cf. Choi et al. 2017; Spydell et al. 2019). A circular cluster has an aspect ratio of one, an ellipsoidal cluster $\alpha < 1$, and a colinear cluster $\alpha \approx 0$.

The estimated kinematic properties are compared to the true model kinematic properties by averaging over the drifter cluster area; for example, for the vorticity $\overline{\zeta_m} \equiv 1/A\int \zeta dA$. We regress the estimate against the "true" values in the numerical model to compute the coefficient of determination R^2, where R is Pearson's correlation coefficient defined as $R = \mathrm{cov}(\mathbf{X}, \mathbf{Y})/[\mathrm{std}(\mathbf{X})\mathrm{std}(\mathbf{Y})]$ for two populations $\mathbf{X}$ and $\mathbf{Y}$. R^2 determines how much of the total variance is captured by the regression model. A second, more practical metric is the rms error of this regression; the vorticity error is $\epsilon_{\mathrm{rms}} = \sqrt{(\zeta - \zeta_m)^2}$, where ζ_m is the area-averaged model vorticity.

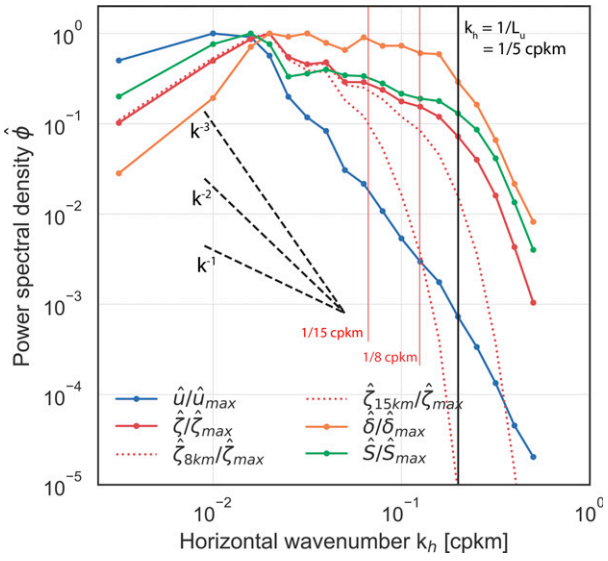

FIG. 3. Wavenumber spectra of the model velocity $|u|$, vorticity ζ, divergence δ, and lateral strain rate S as a function of horizontal wavenumber k_h. Two spatially filtered vorticity fields, 2 and 5 km, are shown with dotted lines. One-dimensional spectra were computed from two-dimensional wavenumber spectra by transformation to polar coordinates and integration over azimuths, and bin averaging into 10 bins per decade. Each spectrum is normalized by its maximum value for better comparison of spectral slopes and rolloffs. Vertical line at $k_h = 1/L_u = 1/5$ cpkm indicates the wavenumber of the original model velocity, above which the kinematic property spectra are smooth, and the red vertical lines indicate $L_u = 8$ km and $L_u = 15$ km of the spatially filtered fields.

All three methods estimate the kinematic properties from the model velocity field (Fig. 4) with high correlations between the estimated and model values; that is, $R^2 = 0.96$. However, even under ideal conditions (i.e., small length scales $L/L_u = 0.2$, and large aspect ratios $\alpha = 1$), the Saucier and Kawai methods produce rms vorticity errors of 0.53 and 0.61, respectively. The sign and magnitude of the vorticity can be predicted, but the Saucier and Kawai methods underestimate the vorticity when the magnitude of the true vorticity is large, perhaps because the largest values occur at the smallest scales. The reason why the Saucier and Kawai methods underpredict vorticity without systematic bias at true zero vorticity may be that they are area-averaged estimators, whereas the LS method performs better at recovering the vorticity.

On the contrary, the LS method produces smaller rms errors, $\epsilon = 0.29$, at the same correlation $R^2 = 0.96$. Especially when the vorticity is small, the LS method appears to perform more robustly. The error dependencies on N, α, and L also hold for lateral strain rate and divergence with similar functional forms (not shown). This is due to the fact that the error here is largely due to nonconstant velocity gradients at and below the cluster length scale L and systematic errors are zero. For the remainder of this section, we use the LS method, which we identify as the most robust method.

b. *Impact of unresolved flow length scales*

To vary the dominant length scale of variability of the velocity field, we filter the model fields with a two-dimensional Gaussian filter resulting in smooth velocity fields below $L_u = 8$ and 15 km (Fig. 3). These are typical length scales at submesoscale fronts (e.g., Hormann et al. 2016). Filtering the model output, by smearing out the vorticity field, might not be equivalent to varying the dominant length scale in evolving simulations and likely produces smoother fields below the filter length scale. Nevertheless, this exercise is illuminating to better understand the uncertainty in drifter cluster-based velocity gradient estimates.

As above, we use the coefficient of determination R^2 and the rms error ϵ_{rms} to evaluate the performance of the estimate (Fig. 5). Figure 5 shows the vorticity fields for the three test cases: the original model run with $\Delta x = \Delta y = 1$ km, the 2-km filtered field, and the 5-km filtered field. The LS estimate of vorticity in all three cases is well correlated with the true vorticity field, with R^2 values ranging from 0.8 to 0.99 and p values below 10^{-4}. As long as the cluster length scales are small relative to the scale of the flow features, the estimates improve and R^2 increases. Analogously, when the cluster length scales are small relative to the scale of a flow features, the rms errors decrease.

The relationship between the rolloff length scale of low-pass filtered model fields and the cluster length scale becomes more explicit in wavenumber spectra. As shown in Fig. 3, filtering removes variability below the filter length scale such that velocity and vorticity fields are smooth. In other words, velocity gradients are constant across drifter clusters, consistent with the LS assumptions of a linear velocity field. The original model fields drop off steeper than k^{-2} below about 5 km. The two filtered fields drop off at 8 or 15 km, respectively, explaining why larger clusters were able to perform better in estimating the velocity gradients.

c. *Sensitivity to shape*

The shape of the drifter clusters significantly influences the estimates of the kinematic properties. In the numerical model, we vary the cluster shapes systematically, compute the kinematic properties, and evaluate the uncertainties.

For each shape configuration with L, α, and N, 10 000 synthetic drifter clusters are randomly positioned and randomly oriented in the model to compute the kinematic properties. The resulting distributions of the estimates allow us to determine the uncertainties and sensitivity to the cluster shapes.

Figure 6 shows the sensitivity of the LS estimates to the shape of the drifter clusters in the model. Each data point represents an experiment with 10 000 model clusters of fixed L, α, and N. As L/L_u increases (Figs. 6a,d), the vorticity errors grow logarithmically. As soon as the drifter clusters become larger than $L/L_u > 2$ and $\epsilon_{\text{rms}} \sim 1$, the estimates become increasingly meaningless as the variability at smaller scales is aliased into the signal. R^2 approximately decreases like $1/L$, suggesting that the kinematic properties can only be estimated

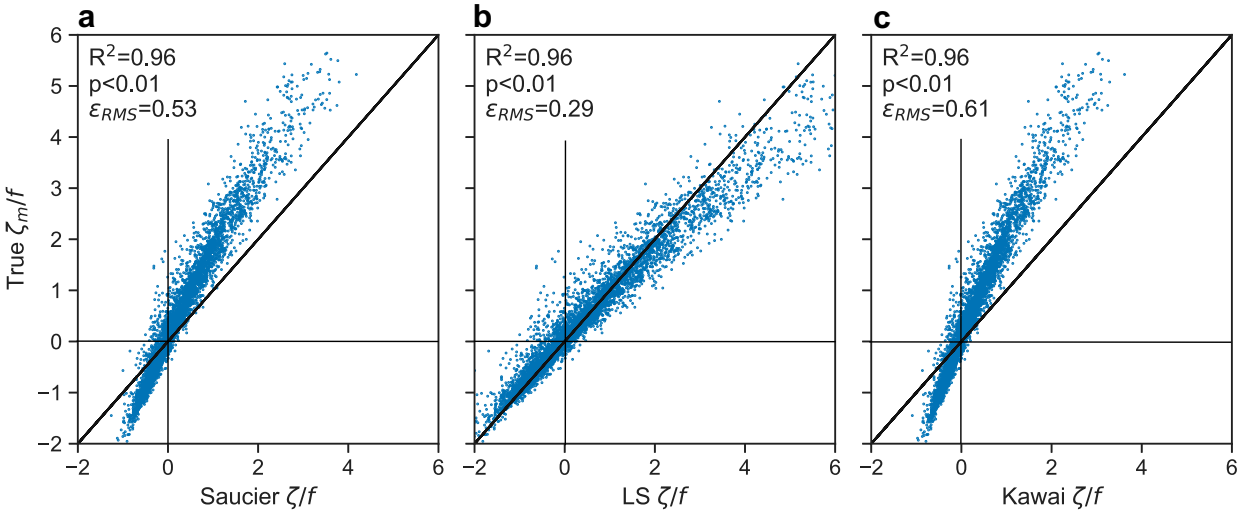

FIG. 4. Comparison of drifter-estimated, normalized vorticity to true model vorticity using (a) the Saucier method based on the area rate of change, (b) the LS method, and (c) the Kawai method based on Stokes's theorem. For each comparison, 10 000 synthetic drifter clusters were released with length scale $L/L_u = 0.2$, aspect ratio $\alpha = 1$, and $N = 6$ drifters per cluster. The coefficient of determination R^2, p value, and rms error ϵ_{rms} are shown in the upper-left corner of each panel.

accurately if the clusters have small length scales that are smaller or approximately equal to L_u.

This relationship becomes clearer when considering the filtered velocity fields in Fig. 5. The linear regression works well if the clusters are smaller than the dominant length scale L_u, resulting in large R^2. The Gaussian filtering removes variability below the filter scale, such that L_u increases. Since L remains unchanged in these comparisons, L/L_u decreases and there is progressively less aliasing or impact of unresolved scales in the filtered cases.

The aspect ratio α also affects the velocity gradient estimates, but to a lesser extent than L/L_u. As the drifter clusters elongate and α decreases, R^2 decreases and ϵ_{rms} increases, particularly in the extreme cases with $\alpha < 0.2$. In addition to the elongation of the clusters, the direction of elongation relative to the direction of the velocity gradients is important. If the clusters are elongated perpendicular to the velocity gradients, the ability to compute the gradients accurately is largely diminished. While this is possible to address in a model, the cluster orientation is challenging to determine in drifter observations because the direction of the velocity gradients is usually not known.

Last, the number of drifters N per cluster theoretically increases the accuracy of the estimates but as N increases, R^2 and ϵ_{rms} show only a weak or no dependence on N (Figs. 6b,c). We find that $N = 3$ is slightly worse than $N = 6$ or 9 but we cannot find a functional dependence. The impact of N, however, might be more pronounced when there is systematic error on the velocity data, which is absent here, because it could reduce the residual using least squares. Okubo and Ebbesmeyer (1976) determined that at least six drifters are needed to yield reasonable results for the vorticity and divergence estimates. It is worth mentioning that although an increase in N reduces the uncertainty of the LS method, this does not imply an increase in accuracy.

d. *Estimating error functions*

Summing up the findings of the previous section, we show in Fig. 6 that the vorticity error increases with L/L_u, where L_u is the decorrelation scale of the velocity field. In Fig. 5, we show that when L_u is increased, for example by low-pass filtering in space or by a shift in dynamic regime in the real ocean, the vorticity estimation improves.

1) EMPIRICAL RESULTS

We can use the sensitivity study and information in Fig. 6 to construct a vorticity error function with independent variables α and L. It consists of saturating functions that are inspired by the theoretical functions derived below:

$$\epsilon(L,\alpha)_{\text{RMS}} = c_0 + c_1 \frac{L_u}{L}\left[1 - \exp\left(-c_2 \frac{L}{L_u}\right)\right] + c_3 \frac{L_u^2}{L^2} \exp\left(-c_4 \frac{L}{L_u}\right) + c_5\left[1 - \exp(-c_6\alpha)\right], \tag{8}$$

where the coefficients ($c_0 = 1.363$, $c_1 = -0.267$, $c_2 = 7.380$, $c_3 = -0.003$, $c_4 = 0.162$, $c_5 = -0.156$, $c_6 = 3.154$) have been determined by least squares fitting and the number of drifters per cluster has been set to $N = 6$.

2) THEORETICAL EXPECTATIONS

The LS method computes an average velocity gradient $\overline{u_x}$. If the true u_x is constant over the drifter cluster, $u_x(x_0) = \overline{u_x}$. If u_x is nonconstant, the LS methods generates errors. Since instrument errors are zero in the numerical model, all errors described in this section and in Fig. 6 are due to nonconstant velocity gradients.

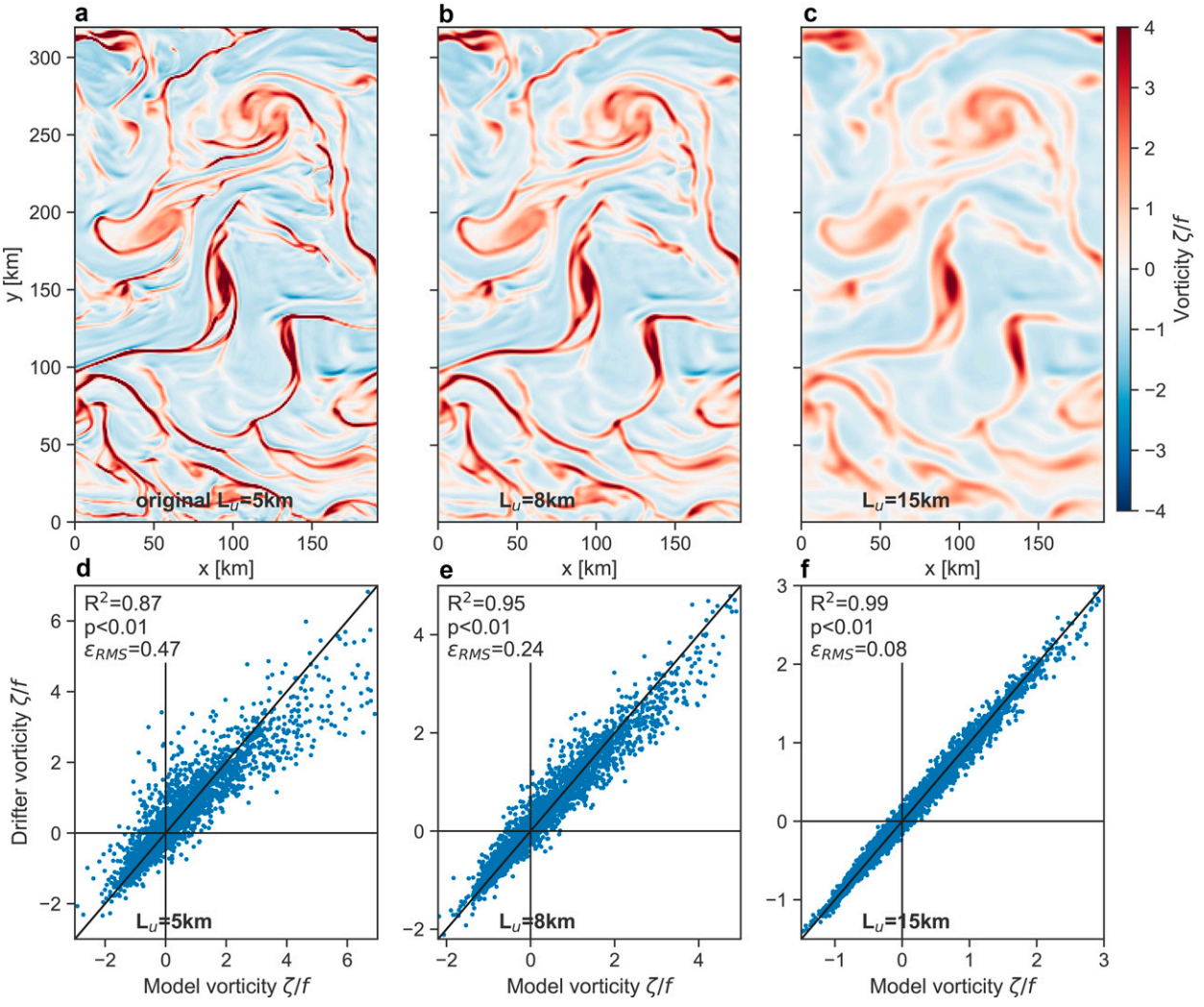

FIG. 5. Vorticity normalized by f of the (a) original simulation with $L_u = 5$ km (as in Fig. 2b) and (b),(c) the Gaussian filtered field with $L_u = 8$ km and $L_u = 15$ km, respectively. (d)–(f) The performance of the LS vorticity estimates using drifters in the 5-km, 8-km filtered, and 15-km filtered model fields. A linear regression between the true model vorticity and estimated vorticity and the rms error ϵ_{rms} are used to evaluate the performance.

For simplicity we consider the LS method as a spatial low-pass filter that computes an average velocity gradient over the length scale of a drifter cluster:

$$\overline{u}_x = \frac{1}{L}\int_{x_0-L/2}^{x_0+L/2}\frac{du}{dx}dx = \frac{1}{L}\left[u\left(x_0+\frac{L}{2}\right)-u\left(x_0-\frac{L}{2}\right)\right]. \quad (9)$$

If we assume that the velocity gradient $u_x(x_0)$ is distributed with a covariance function $C(n) \equiv \langle u_x(x_0)u_x(x+n)\rangle$, so that the lagged correlation function is $\rho_{u_xu_x} = C(n)/\langle u_x^2\rangle$, we can compute statistics on the average velocity gradient. The other components of the two-dimensional velocity gradient are assumed to behave analogously.

Using the expression above, the variance of the LS velocity gradient can be rewritten using the expression for the variance as

$$\langle[\overline{u_x}(x_0)]^2\rangle = \frac{1}{L}\int_{x_0-L/2}^{x_0+L/2}\int_{x_0-L/2}^{x_0+L/2}\frac{du(x_1)}{dx_1}\frac{du(x_2)}{dx_2}\,dx_1dx_2, \quad (10)$$

$$= \frac{4\langle u_x^2\rangle}{L^2}\int_0^{L/\sqrt{2}}\int_0^{L/\sqrt{2}-s}\rho_{u_xu_x}(n)dnds. \quad (11)$$

The correlation between estimated $\overline{u_x}$ and true u_x is

$$\langle\overline{u_x}(x_0)u_x(x_0)\rangle = \frac{1}{L}\int_{x_0-L/2}^{x_0+L/2}\frac{du}{dx}\,dx, \quad (12)$$

$$= \frac{2\langle u_x^2\rangle}{L}\int_0^{L/2}\rho_{u_xu_x}(n)dn. \quad (13)$$

Assuming a covariance function $C(n) = \exp(-|n|/L_u)$, where L_u is the flow decorrelation scale, we can solve for the variance and correlation, respectively:

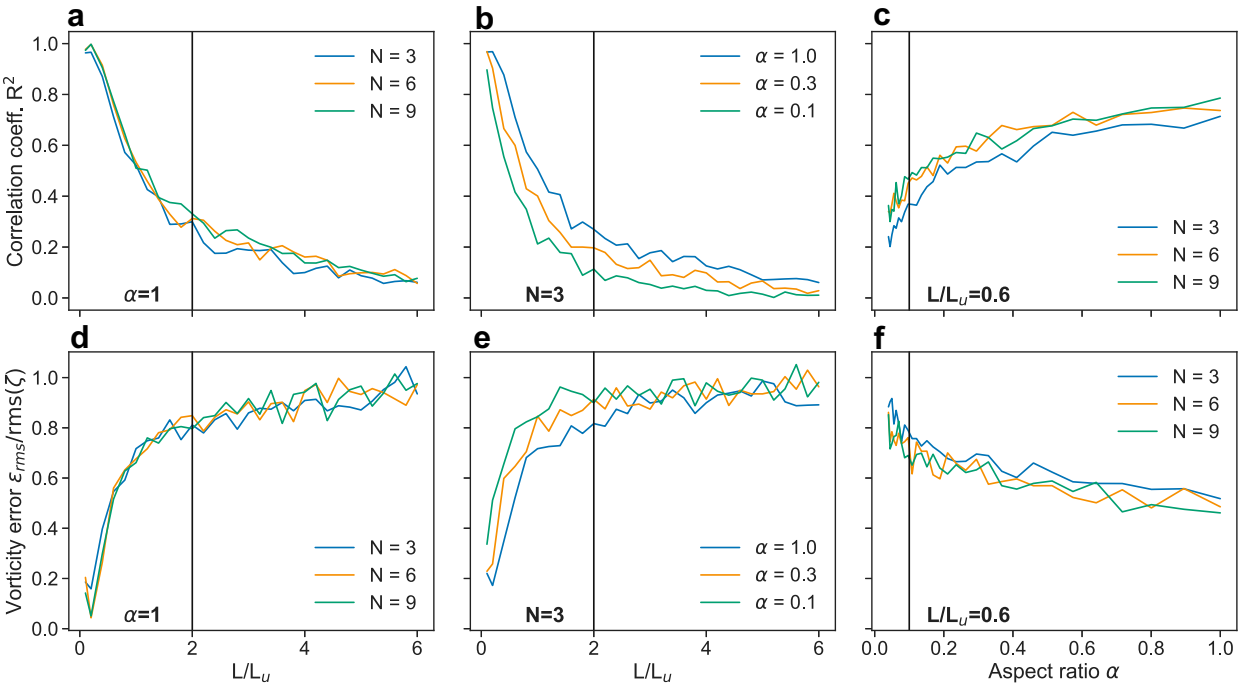

FIG. 6. Sensitivity analysis of the vorticity estimates based on drifter cluster shape. Each parameter set, consisting of normalized length scale L/L_u where L_u is set to 5 km, aspect ratio α, and number of drifters N, was used to estimate the vorticity from 10 000 synthetic clusters. (a)–(c) The coefficients of determination R^2. (d)–(f) The rms errors ϵ_{rms} normalized by the rms vorticity rms(ζ) between the modeled and estimated vorticities. Black vertical lines indicate the parameter limits, $L/L_u = 2$ and $\alpha = 0.1$, used in the analysis of the observational drifter data in section 4.

$$\langle[\overline{u_x}(x_0)]^2\rangle = \frac{4\langle u_x^2\rangle L_u^2}{L^2}\left[\frac{L}{\sqrt{2}L_u} + \exp\left(\frac{L}{\sqrt{2}L_u}\right) - 1\right], \tag{14}$$

$$\langle\overline{u_x}(x_0)u_x(x_0)\rangle = \frac{2\langle u_x^2\rangle L_u}{L}\left[1 - \exp\left(\frac{L}{\sqrt{2}L_u}\right)\right]. \tag{15}$$

The rms error is a combination of the two functions 11 and 13 above:

$$\begin{aligned}\epsilon_{\text{RMS}} &= \langle[\overline{u_x}(x_0) - u_x(x_0)]^2\rangle \\ &= \langle[\overline{u_x}(x_0)]^2\rangle - 2\langle\overline{u_x}(x_0)u_x(x_0)\rangle + \langle u_x^2\rangle.\end{aligned} \tag{16}$$

In Fig. 7, the variance, correlations and rms errors are shown as a function of L. At large L/L_u, that is, when the cluster length scale is much larger than the flow decorrelation scale, the error saturates. The rms error asymptotes to the total velocity gradient variance. At small L/L_u, the mean variance and correlation decrease like $1/L$ and the rms error increases like L. A similar behavior has been observed in the empirical curves suggesting that L/L_u is the dominant parameter with much larger influence on the error and correlation than α and N (Fig. 7c). The mismatch in magnitude between theoretical and empirical might stem from the fact that the theoretical curves are only derived for one-dimensional gradients and an symmetric covariance function around zero.

The theoretical considerations here show that the primary sources of error are nonconstant velocity gradients below the scale of a drifter cluster. When the background gradient is not constant across a cluster, that is, if $u(x + x', y + y') \neq \overline{u}(x, y) + u_x(x, y)x' + u_y(x, y)y'$, the accuracy is limited by the LS assumption being violated and not by the noise.

4. Application to drifter observations

For the subsequent analysis of the SVP drifters in the Bay of Bengal using the LS method, we choose $N = 6$ drifters per cluster as a compromise between horizontal resolution and availability of clusters that meet the aspect-ratio and length scale criteria (cf. Okubo and Ebbesmeyer 1976). These criteria suggest that submesoscale flows will not be sufficiently resolved for too large $L/L_u > 2$ and $\alpha < 0.1$. If we assume that $L_u = 5$ km like in the numerical model and require $L/L_u < 2$ we arrive at a maximum length scale of $L = 10$ km which has also been estimated based on a cross-correlation analysis in Hormann et al. (2016) and a pair dispersion analysis in Essink et al. (2019). It is likely an upper bound for submesoscale flows, but might not be for the resolved velocity gradients. These two conditions are only met during the first few days after the drifter deployments.

a. *Error due to GPS uncertainty*

The velocity error due to GPS uncertainty σ_{uv} will cause additional uncertainties in the kinematic property calculations.

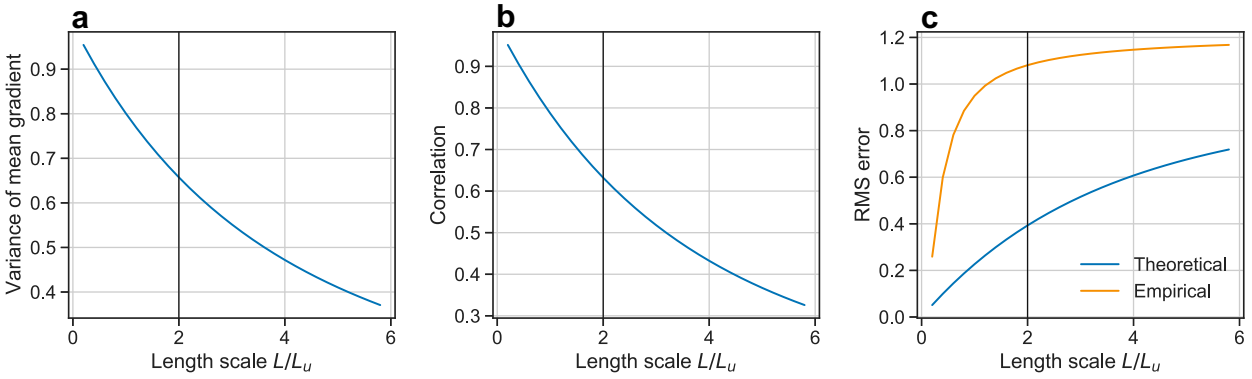

FIG. 7. Theoretical predictions from sampling a known, space-lagged covariance function of velocity gradients for (a) variance $\langle[\overline{u_x}(x_0)]^2\rangle$, (b) correlation $\langle\overline{u_x}(x_0)u_x(x_0)\rangle$, and (c) rms error ϵ_{RMS} as estimated in Eqs. (14)–(16). In (c), the empirical error from fitting to the numerical results is also plotted. All quantities are normalized by the total variance $\langle u_x^2\rangle$. These curves should be compared to Fig. 6. The vertical black lines indicate the L/L_u threshold above which the rms error saturates at its maximum.

Spydell et al. (2019) determined from stationary GPS beacons how σ_{uv} affects the vorticity error for a drifter cluster:

$$\sigma_\zeta = \sqrt{\frac{\sigma_{uv}^2}{\lambda_{\min}^2 N}\left(1+\frac{\lambda_{\min}^2}{\lambda_{\max}^2}\right)(1-\rho_{uv})}, \tag{17}$$

where $\lambda_{\min}$ and $\lambda_{\max}$ are the lengths of the minor and major axes of the drifter cluster, $\alpha = \lambda_{\min}/\lambda_{\max}$ the cluster's aspect ratio, N the number of drifters per cluster, and ρ_{uv} the correlation coefficient between velocities derived from different GPS beacons. We can safely assume $\rho_{uv} = 0$ to simplify the expression, so that σ_ζ^2 will be an upper bound for the vorticity error variance.

Drifter GPS accuracy of the position improves with runtime but the position components stabilize with a rms error of $\sigma_x \approx 5$ m after several minutes. The propagation of position uncertainties yields estimates of the velocity errors of $\sigma_{uv} \approx 0.01$ m s^{-1} (cf. Hormann et al. 2016; Maximenko et al. 2013; Centurioni 2018). For a regular (i.e., $\alpha = 1$) six-drifter cluster of $L = 5$ km, the vorticity error due to GPS uncertainty is about $\sigma_\zeta = 0.03f$ while an elongated cluster with $\alpha = 0.1$ gives $\sigma_\zeta = 0.2f$. For small aspect ratios $\alpha < 0.1$, the GPS uncertainty becomes large; that is, as large as the estimated eddy vorticity which is consistent with our findings for the method error ϵ_{RMS} determined above.

The error variability due to GPS uncertainty, within the range of scales and aspect ratios considered here, is lower than that of the rms error computed for each method above, which varies between 0 and $1f$. Only when method uncertainty is low, the GPS uncertainty will control the total error. The GPS error function (17) increases with α and decreases with N and L.

b. Cluster geometry

The kinematic properties will be computed on clusters with $N = 6$ drifters. There are over 8 million possible combinations for 45 drifters, every 5 min. Reducing this number in a physically meaningful way is a challenge to large drifter releases and has computational relevance. In this study, we filter all combinations in space with the length scale and aspect-ratio criteria described above; that is, $L/L_u < 2$ and $\alpha > 0.1$.

On average, the drifter cluster sizes grow monotonically over the first month after deployment in the Bay of Bengal (Fig. 8a). The mean length scale L initially grows rapidly (approximately as $e^{0.2t}$). Here, the most energetic motions are mesoscale eddies that are about 100 km in diameter, larger than the deformation radius $L_D = 60$ km. The initial 3–4 days after deployment suggest exponential growth, consistent with the nonlocal regime found using pair dispersion statistics (cf. Essink et al. 2019). Similar behavior and an analogy to pair dispersion was found by LaCasce and Ohlmann (2003), who derived an expression to relate pair separations to cluster length scales.

After deployment at $t = 0$ days, when a large fraction of the drifter clusters has an aspect ratio of $\alpha < 0.5$, the clusters elongate dramatically (Fig. 8b) as drifters wrap around the perimeter of the dominant mesoscale eddy (Fig. 1c), the length scales increase and the aspect ratios collapse most rapidly. Within 2 days, the clusters stretch out until at least 75% have an aspect ratio of $\alpha < 0.1$, equivalent to a major axis 10 times larger than the minor axis. The exponential e-folding time with which this occurs is about two days, roughly consistent with the e-folding time scale computed from drifter-pair statistics (Essink et al. 2019). LaCasce and Ohlmann (2003) observed a similar change in cluster aspect ratios for drifters in the Gulf of Mexico. Their aspect ratio, defined as the ratio of the base and height of a triangle, becomes on the order of 10 (approximately inverse of α) with a time scale of 2 days.

Based on the sensitivity analysis (section 3), the ensemble-mean L and α (Fig. 8) predict low coefficients of determination R^2 and large rms errors ϵ_{RMS} for the estimated velocity gradients. Three additional challenges for drifters in the ocean can be hypothesized: (i) small-scale variability, with nonconstant velocity gradients across the cluster-scale L will violate the LS assumptions, (ii) velocity correlations between pairs and clusters of drifters decrease substantially within only a few days (cf. Beron-Vera and LaCasce 2016; Essink et al. 2019),

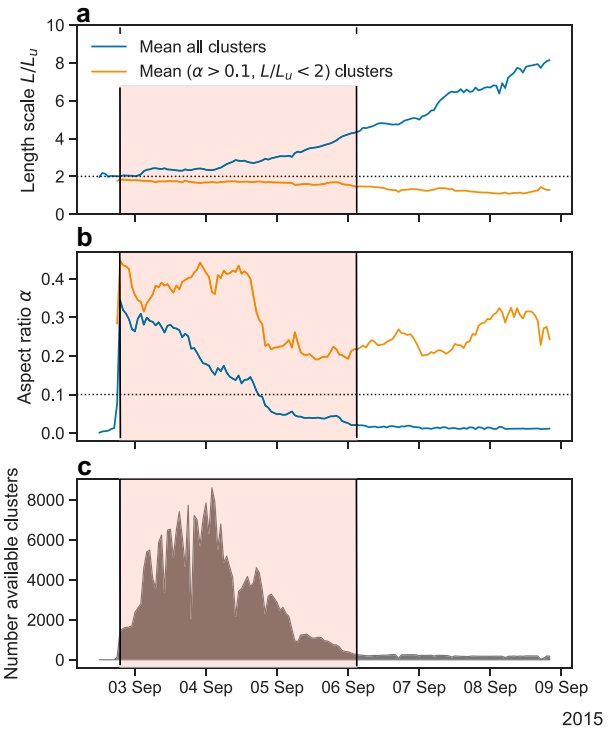

FIG. 8. Time evolution of (a) mean length scales L/L_u and (b) mean aspect ratios α of all ($N = 6$) (blue) and selected (yellow) ($\alpha > 0.1$, $L/L_u < 2$) in the Bay of Bengal. (c) Number of available clusters that fulfill the criteria ($\alpha > 0.1$, $L/L_u < 2$). The shaded regions shows the 3-day window favorable for further analysis with enough clusters available to obtain meaningful statistics.

and (iii) position and velocity measurements will be subject to noise. Therefore, the estimation of the kinematic properties can only be successful for a few days after deployment.

c. *Composite maps of kinematic properties*

By spatially binning the drifter-derived kinematic properties, we map vorticity, lateral strain rate, and divergence in space. The longitudinal and latitudinal length scales of each bin are chosen to be 10 km, consistent with Hormann et al. (2016) and Essink et al. (2019) and equal to $2L_u$. The median of all data in each latitude–longitude bin is shown in color in Fig. 9. This binning procedure reduces the degree of redundancy because individual drifters can be part of multiple clusters. Plotting maps of the kinematic properties presumes that the vorticity, divergence, and strain rate vary slowly over the chosen ~3-day period. The near-surface density estimates from the drifters are also shown in Fig. 9a. Consistent with other observations during the 2015 ASIRI field experiment, the freshwater-dominated density front stands out in the spatial maps. Relatively fresh waters originating from rivers and rain in the northern bay are advected southward in plumes and stirred by mesoscale eddies.

The vorticity and lateral strain rate maps reflect the north–south pattern in the density gradients (Figs. 9b,d,f). A sharp change of the vorticity values and sign occurs where the density transitions from denser to fresher waters, with the largest values of vorticity and lateral strain rate occurring at the edge of the density front. The vorticity distribution across the density front is consistent with a frontal jet in geostrophic balance, with negative vorticity on the lighter side and positive vorticity on the denser side of the front. This agreement between the density and vorticity patterns is robust since the density is derived from drifter sensor measurements while the kinematic properties are independently estimated from the drifters' GPS positions. The divergence shows a less clear pattern when plotted in space. However, some of the structures are consistent with the vorticity and lateral strain rate fields.

The large-scale patterns further show the dominant cyclonic mesoscale eddy that was present during the period of the experiment (see Fig. 1c), which is also reflected in the drifter trajectories (cf. Hormann et al. 2016; Essink et al. 2019). Within the eddy, the vorticity field is mostly positive, especially at later times during the drifter experiment, when the influence of the density gradients weakens (see Fig. 9b). The cyclonic background vorticity likely biases the cluster-scale vorticity estimates, particularly when the small-scale vorticity is weak. Furthermore, a positively skewed vorticity distribution is expected as observed in previous experiments (e.g., Rudnick 2001; Shcherbina et al. 2013).

During the first few days, we observe a banded pattern in the vorticity and divergence maps that is not reflected in the density field (see Figs. 9b,d). This banded pattern has a horizontal wavelength of approximately 30 km, about $0.1f$ amplitude, and alternating positive and negative values with vorticity leading divergence by about 6–12 h. Although challenging to pinpoint with this dataset considering the Lagrangian space–time aliasing of spatial maps, this is likely due to diurnal heating and cooling of the surface ocean and an associated diurnal pattern of the eddy viscosity (e.g., Thushara and Vinayachandran 2014). Changes in the eddy viscosity in the surface layer modulate the ageostrophic frontogenetic flow, and thus the horizontal divergence. Previous experiments have attributed this phenomenon to frontal adjustment to the turbulent thermal wind balance (Dauhajre and McWilliams 2018; McWilliams 2016) and recent observations and simulations in the Gulf of Mexico provide similar evidence (e.g., Johnson et al. 2020a,b).

d. *Temporal variability*

Figure 10 shows time series of the kinematic properties computed as the mean of all drifter clusters available at each point in time. Before computing the mean time series over all clusters, the time series of each cluster are filtered with a 4-h running mean to focus on the diurnal and submesoscale variability and to remove high-frequency noise. The time series of the kinematic properties show high variability as indicated by the confidence intervals plotted around the mean values (Fig. 10). The tails of the distributions at each instant in time, particularly for submesoscale currents, reach $\mathcal{O}(f)$ vorticity and lateral strain rate magnitudes. Since the drifter clusters traveled as a coherent group during the initial phase of the experiment, sampled similar flow features, and drifter velocities are correlated

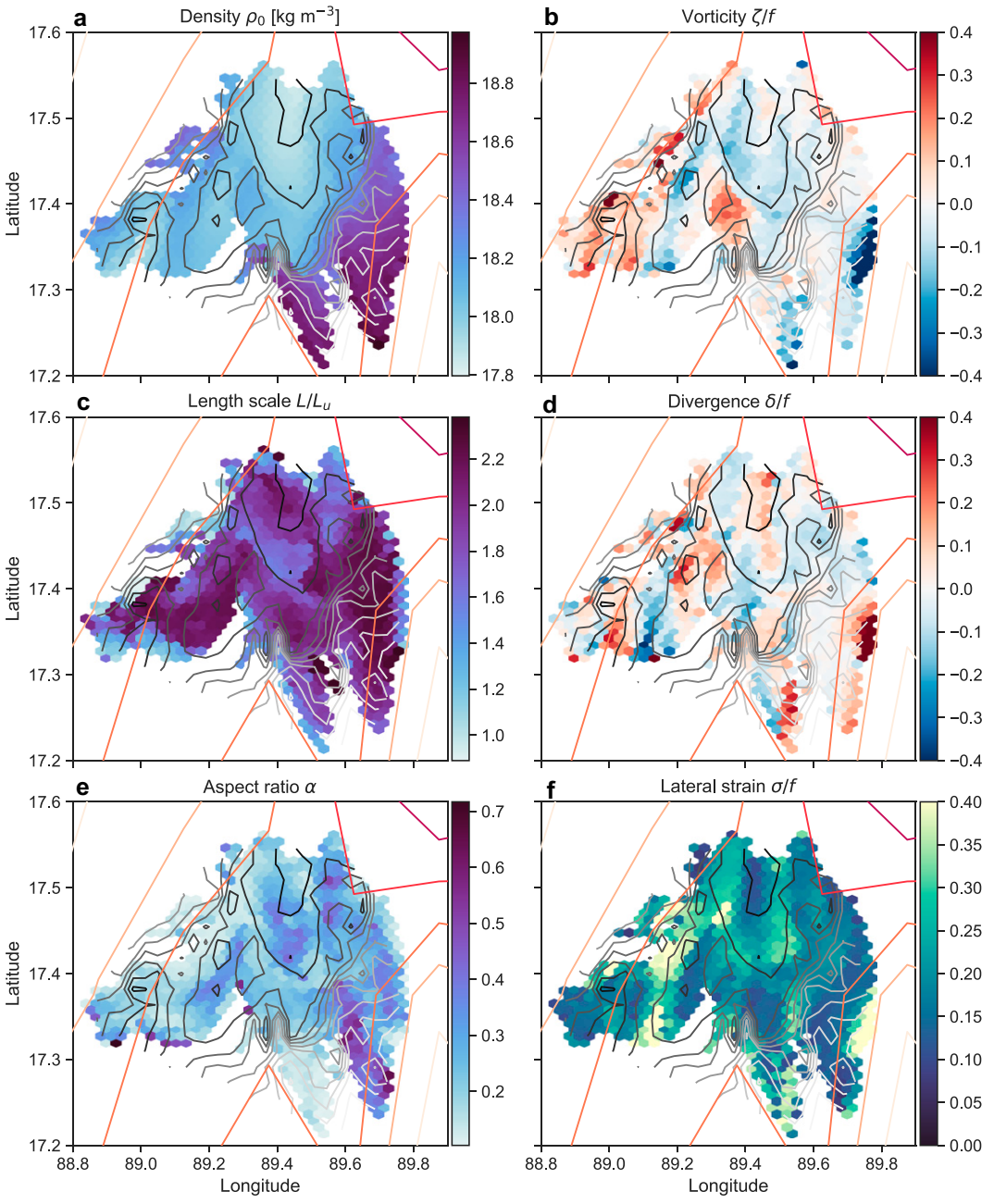

FIG. 9. Composite spatial maps over 3 days after the drifter deployments (i.e., 3–6 Sep 2015) of (a) density anomaly ρ_0, (b) vertical vorticity ζ/f, (c) length scale L/L_u, (d) divergence δ/f, (e) aspect ratio α, and (f) lateral strain rate σ/f. Maps show the median value of latitude–longitude (5 km × 5 km) hexagonal bins containing at least three data points. Overlaid are contours of the density anomaly ρ_0 in gray that are also shown in (a) and contours of sea surface salinity from SMAP (4 Sep 2015).

(Essink et al. 2019), computing such time series is a reasonable approach.

Since the divergence is the difference of two large horizontal-shear terms, its estimation is often noisier and produces larger uncertainties than estimates of vorticity. Systematic errors such as from GPS uncertainty can therefore significantly deteriorate divergence estimates (Spydell et al. 2019) (see section 4a). The confidence in vorticity estimates is more robust since they tend to be of larger magnitude than the divergence relative to the magnitude of errors (Paduan and Niiler 1990). In the past, the shallow water vorticity equation, neglecting wind stress at the surface, was used to infer the divergence from time series of vorticity (e.g., Paduan and Niiler 1990; Swenson et al. 1992):

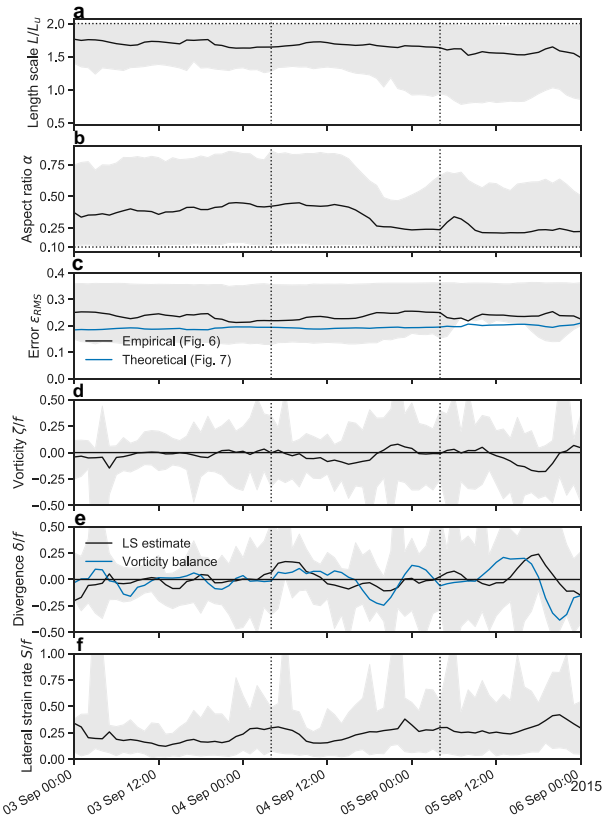

FIG. 10. A 3-day time series of the drifter experiment for the period 3–6 Sep 2015 showing (a) the mean length scale L/L_u, where $L_u = 5$ km, (b) the mean aspect ratio, (c) the theoretical and empirical error calculated from section 3d, (d) the mean vertical vorticity ζ/f, (e) the mean divergence δ/f, and (f) the mean lateral strain rate S/f. The shaded regions indicate the 95% confidence interval determined directly from the distribution of estimates for each cluster. Vertical dotted lines indicate 24-h periods, and horizontal dotted lines indicate $L/L_u < 2$ and $\alpha > 0.1$.

$$\frac{D(\zeta + f)}{Dt} + (\zeta + f)\delta = 0, \tag{18}$$

where δ is the horizontal gradient of the velocity as defined previously, which is the term for the stretching of columns of the absolute vorticity $f + \zeta$.

In our drifter dataset, the divergence estimates from the shallow water vorticity equation agree well with the estimated divergence from the drifter clusters during the initial deployment phase (Fig. 10). During this period, the drifter clusters are still small and regular, and the kinematic property estimates are expected to be reliable. The consistency between the estimates using the shallow water potential vorticity equation and the independent estimates using the LS method demonstrates the robustness of our divergence estimates.

Periodic patterns at diurnal period occur in all three kinematic properties. Most notably, the alternating peaks and troughs in the vorticity and divergence mirror the banded patterns observed in the spatial maps (Fig. 10). Diurnal cycling of vorticity and divergence is related to adjustment to the turbulent thermal wind balance and arises at restratifying fronts (Johnson et al. 2020a,b). It has recently been described in both observations and modeling studies (Dauhajre and McWilliams 2018; Sun et al. 2020). An Ekman layer in a lateral density gradient, such as the front observed here, has an ageostrophic flow which is frontogenetic. If the viscosity is modulated by the diurnal cycle, then the frontogenesis rate and convergence are also modulated (Wenegrat and McPhaden 2016; McWilliams 2016).

Other processes such as inertial oscillations and tides are unlikely to create this variability. Barotropic tides in the region are dominated by semidiurnal constituents and generally weak, so unlikely to generate diurnal peak-to-peak vorticity fluctuations of $\mathcal{O}(f)$. Inertial motions have a period of about 20 h at 17°N, which is far from diurnal even when considering the shift to higher frequencies due to the $0.2f$ cyclonic eddy vorticity.

The decreasing magnitude of the fluctuations can be attributed to the fact that the clusters become larger over time (Fig. 8) or that the amplitude of atmospheric forcing weakens. Although overcast and rapidly passing storm systems are common in the waning monsoon season, the wind speed and direction did not change over the experiment period presented here. Large clusters act like a spatial low-pass filter on the vorticity signal (as discussed above), therefore reduce the magnitude, and smear out flow features. Figure 8 suggests that the average cluster length scale increased to 40 km in about three days, which could account for the decrease in kinematic property fluctuations. In addition, the aspect ratios also tend to become small after a few days, decreasing confidence in the late-time behavior. After 3–4 days the kinematic properties not only become unreliable but also reflect vastly larger scales than the frontal and mesoscale processes described above.

5. Summary and conclusions

We evaluated three methods to estimate kinematic properties from drifter clusters in a numerical model and applied the findings to a drifter dataset collected in the Bay of Bengal.

Our analyses indicate that the LS method proposed by Okubo and Ebbesmeyer (1976) and Molinari and Kirwan (1975) provides the most robust results. Using synthetic drifters in a model flow field, we find that the cluster length scale L and aspect ratio α have the largest impact on the uncertainties, likely caused by (i) violation of the linear assumption of the LS method by inhomogeneous velocity gradients across drifter clusters and (ii) aliasing of unresolved scales (and the fact that variance of velocity gradients might increase at small scales). The magnitude of those errors becomes large [i.e., $\mathcal{O}(f)$] as soon as the drifter clusters are too elongated or too large to resolve the variability in the flow field.

Clusters with small aspect ratios $\alpha < 0.1$ cause the largest errors. Therefore, regions of greatest interest like submesoscale fronts are challenging to measure because this is where convergence and horizontal shear are strongest, leading to substantial deformation and elongation of the drifter clusters.

Uncorrelated velocity noise also impacts the kinematic property estimates (Spydell et al. 2019). The total known uncertainty is the sum of rms errors due to the method and GPS uncertainties $\epsilon = \epsilon_{\mathrm{RMS}} + \sigma_\zeta$. The kinematic property error σ_ζ due to GPS uncertainty increases with α and decreases with L and N. Although the GPS uncertainty [i.e., $\mathcal{O}(0.1)f$] is smaller than the method uncertainty for the observations presented here, higher-accuracy GPS algorithms will improve our ability to do these calculations (Haza et al. 2014; Spydell et al. 2019).

Drifters in the Bay of Bengal measured positively skewed vorticity with maximum values of f, negatively skewed divergence with minimum values of $-f$, and collocated lateral strain rate with maximum values of f. These are consistent with shipboard measurements in the region and reflect the influence of a prevailing cyclonic mesoscale eddy as well as a north–south density front.

At the perimeter of the eddy, a banded pattern parallel to the front with a diurnal period and a horizontal wavelength of about 20 km was observed. The freshwater-dominated front was likely intensified due to shear at the perimeter of the cyclonic eddy. Adjustment to the turbulent thermal wind balance generates banded patterns as a response to diurnal surface forcing and an associated change in surface viscosity. Ongoing investigations within the MISO-BOB program will elucidate further details of the diurnal variability in the Bay of Bengal (Shroyer et al. 2021).

Numerical modeling and observational data were combined to provide guidance on which drifter clusters are useful for the computation of velocity gradients and which can be sorted out. As a result, we propose practical criteria for length scales and aspect ratios that can serve as reference for future studies.

Improvements can be made with enhanced GPS accuracy, larger numbers of independent drifter trajectories, and shallower drogue depths with the caveat of introducing more noise due to wind and waves (Poulain et al. 2022). The dependence of the trajectories on initial conditions calls for repeat deployments which will increase confidence in the statistics of associated kinematic properties.

This study complements the insights gained from the first estimates of the kinematic properties using the Saucier method (Hormann et al. 2016) as well as pair dispersion statistics in the submesoscale range (Essink et al. 2019) based on the used drifter dataset. More work is needed to use multidrifter analyses to further constrain submesoscale flow conditions and, in particular, retrieve information on the dynamics at submesoscales.

Acknowledgments. This research was supported by the Office of Naval Research (ONR) Departmental Research Initiative ASIRI under Grant N00014-13-1-0451 (SE and AM) and Grant N00014-13-1-0477 (VH and LC). The authors thank the captain and crew of the R/V *Roger Revelle*, and Andrew Lucas with the Multiscale Ocean Dynamics group at the Scripps Institution for Oceanography for providing the FastCTD data collected in 2015, which was supported by ONR Grant N00014-13-1-0489, as well as Eric D'Asaro for helpful discussions and Lance Braasch for assistance with the drifter dataset. AM and SE further thank NSF (Grant OCE-I434788) and ONR (Grant N00014-16-1-2470) for support. VH and LC were additionally supported by ONR Grants N00014-15-1-2286, N00014-14-1-0183, N00014-19-1-26-91 and NOAA Global Drifter Program (GDP) Grant NA15OAR4320071. The authors are grateful for contributions and constructive feedback from three anonymous reviewers.

Data availability statement. The altimeter products were produced and distributed by CMEMS (https://marine.copernicus.eu), and SMAP data were produced and distributed by NASA JPL PO.DAAC (https://podaac.jpl.nasa.gov). The drifters were released as part of the GDP and their data are available at www.aoml.noaa.gov/phod/gdp.

REFERENCES

Beron-Vera, F. J., and J. H. LaCasce, 2016: Statistics of simulated and observed pair separations in the Gulf of Mexico. *J. Phys. Oceanogr.*, **46**, 2183–2199, https://doi.org/10.1175/JPO-D-15-0127.1.

Berta, M., A. Griffa, T. M. Özgökmen, and A. C. Poje, 2016: Submesoscale evolution of surface drifter triads in the Gulf of Mexico. *Geophys. Res. Lett.*, **43**, 11 751–11 759, https://doi.org/10.1002/2016GL070357.

Callies, J., and R. Ferrari, 2013: Interpreting energy and tracer spectra of upper-ocean turbulence in the submesoscale range (1–200 km). *J. Phys. Oceanogr.*, **43**, 2456–2474, https://doi.org/10.1175/JPO-D-13-063.1.

Centurioni, L. R., 2018: Drifter technology and impacts for sea surface temperature, sea-level pressure, and ocean circulation studies. *Observing the Oceans in Real Time*, Springer Oceanography, Vol. 19, Springer, 37–57.

Choi, J., A. Bracco, R. Barkan, A. F. Shchepetkin, J. C. McWilliams, and J. M. Molemaker, 2017: Submesoscale dynamics in the northern Gulf of Mexico. Part III: Lagrangian implications. *J. Phys. Oceanogr.*, **47**, 2361–2376, https://doi.org/10.1175/JPO-D-17-0036.1.

Dauhajre, D. P., and J. C. McWilliams, 2018: Diurnal evolution of submesoscale front and filament circulations. *J. Phys. Oceanogr.*, **48**, 2343–2361, https://doi.org/10.1175/JPO-D-18-0143.1.

Ducet, N., P. Y. Le Traon, and G. Reverdin, 2000: Global high-resolution mapping of ocean circulation from TOPEX/Poseidon and ERS-1 and -2. *J. Geophys. Res.*, **105**, 19 477–19 498, https://doi.org/10.1029/2000JC900063.

Entekhabi, D., and Coauthors, 2010: The Soil Moisture Active Passive (SMAP) mission. *Proc. IEEE*, **98**, 704–716, https://doi.org/10.1109/jproc.2010.2043918.

Essink, S., V. Hormann, L. R. Centurioni, and A. Mahadevan, 2019: Can we detect submesoscale motions in drifter pair dispersion? *J. Phys. Oceanogr.*, **49**, 2237–2254, https://doi.org/10.1175/JPO-D-18-0181.1.

Fahrbach, E., C. Brockmann, and J. Meincke, 1986: Horizontal mixing in the Atlantic Equatorial Undercurrent estimated from drifting buoy clusters. *J. Geophys. Res.*, **91**, 10 557–10 565, https://doi.org/10.1029/JC091iC09p10557.

Haza, A. C., T. M. Özgökmen, A. Griffa, A. C. Poje, and M. P. Lelong, 2014: How does drifter position uncertainty affect ocean dispersion estimates? *J. Atmos. Oceanic Technol.*, **31**, 2809–2828, https://doi.org/10.1175/JTECH-D-14-00107.1.

Hormann, V., L. R. Centurioni, and G. Reverdin, 2015: Evaluation of drifter salinities in the subtropical North Atlantic. *J. Atmos. Oceanic Technol.*, **32**, 185–192, https://doi.org/10.1175/JTECH-D-14-00179.1.

——, ——, A. Mahadevan, S. Essink, E. A. D'Asaro, and B. P. Kumar, 2016: Variability of near-surface circulation and sea surface salinity observed from Lagrangian drifters in the northern Bay of Bengal during the waning 2015 southwest monsoon. *Oceanography*, **29** (2), 124–133, https://doi.org/10.5670/oceanog.2016.45.

Horstmann, J., J. C. N. Borge, J. Seemann, R. Carrasco, and B. Lund, 2015: Wind, wave, and current retrieval utilizing X-band marine radars. *Coastal Ocean Observing Systems*, Elsevier, 281–304.

Jaeger, G. S., and A. Mahadevan, 2018: Submesoscale-selective compensation of fronts in a salinity-stratified ocean. *Sci. Adv.*, **4**, e1701504, https://doi.org/10.1126/sciadv.1701504.

Johnson, L., C. M. Lee, E. A. D'Asaro, L. Thomas, and A. Shcherbina, 2020a: Restratification at a California Current upwelling front. Part I: Observations. *J. Phys. Oceanogr.*, **50**, 1455–1472, https://doi.org/10.1175/JPO-D-19-0203.1.

——, ——, ——, J. O. Wenegrat, and L. N. Thomas, 2020b: Restratification at a California Current upwelling front. Part II: Dynamics. *J. Phys. Oceanogr.*, **50**, 1473–1487, https://doi.org/10.1175/JPO-D-19-0204.1.

Karimova, S., and M. Gade, 2016: Improved statistics of sub-mesoscale eddies in the Baltic Sea retrieved from SAR imagery. *Int. J. Remote Sens.*, **37**, 2394–2414, https://doi.org/10.1080/01431161.2016.1145367.

Kawai, H., 1985a: Scale dependence of divergence and vorticity of near-surface flows in the sea: Part 1. Measurements and calculations of area-averaged divergence and vorticity. *J. Oceanogr. Soc. Japan*, **41**, 157–166, https://doi.org/10.1007/BF02111115.

——, 1985b: Scale dependence of divergence and vorticity of near-surface flows in the sea: Part 2. Results and interpretation. *J. Oceanogr. Soc. Japan*, **41**, 167–175, https://doi.org/10.1007/BF02111116.

Kirincich, A. R., 2016: The occurrence, drivers, and implications of submesoscale eddies on the Martha's Vineyard inner shelf. *J. Phys. Oceanogr.*, **46**, 2645–2662, https://doi.org/10.1175/JPO-D-15-0191.1.

——, S. J. Lentz, J. T. Farrar, and N. K. Ganju, 2013: The spatial structure of tidal and mean circulation over the inner shelf south of Martha's Vineyard, Massachusetts. *J. Phys. Oceanogr.*, **43**, 1940–1958, https://doi.org/10.1175/JPO-D-13-020.1.

Kirwan, A. D., 1988: Notes on the cluster method for interpreting relative motions. *J. Geophys. Res.*, **93**, 9337–9339, https://doi.org/10.1029/JC093iC08p09337.

Kunze, E., M. G. Briscoe, and A. J. Williams, 1990: Interpreting shear and strain fine structure from a neutrally buoyant float. *J. Geophys. Res.*, **95**, 18 111–18 125, https://doi.org/10.1029/JC095iC10p18111.

LaCasce, J. H., and C. Ohlmann, 2003: Relative dispersion at the surface of the Gulf of Mexico. *J. Mar. Res.*, **61**, 285–312, https://doi.org/10.1357/002224003322201205.

Large, W. G., J. C. McWilliams, and S. C. Doney, 1994: Oceanic vertical mixing: A review and a model with a nonlocal boundary layer parameterization. *Rev. Geophys.*, **32**, 363–403, https://doi.org/10.1029/94RG01872.

Lien, R.-C., and P. Müller, 1992: Normal-mode decomposition of small-scale oceanic motions. *J. Phys. Oceanogr.*, **22**, 1583–1595, https://doi.org/10.1175/1520-0485(1992)022<1583:NMDOSS>2.0.CO;2.

Lucas, A. J., and Coauthors, 2014: Mixing to monsoons: Air-sea interactions in the Bay of Bengal. *Eos, Trans. Amer. Geophys. Union*, **95**, 269–270, https://doi.org/10.1002/2014EO300001.

Lund, B., H. C. Graber, and R. Romeiser, 2012: Wind retrieval from shipborne nautical X-band radar data. *IEEE Trans. Geosci. Remote Sens.*, **50**, 3800–3811, https://doi.org/10.1109/TGRS.2012.2186457.

Mahadevan, A., and A. Tandon, 2006: An analysis of mechanisms for submesoscale vertical motion at ocean fronts. *Ocean Modell.*, **14**, 241–256, https://doi.org/10.1016/j.ocemod.2006.05.006.

——, J. Oliger, and R. Street, 1996a: A nonhydrostatic mesoscale ocean model. Part I: Well-posedness and scaling. *J. Phys. Oceanogr.*, **26**, 1868–1880, https://doi.org/10.1175/1520-0485(1996)026<1868:ANMOMP>2.0.CO;2.

——, ——, and ——, 1996b: A nonhydrostatic mesoscale ocean model. Part II: Numerical implementation. *J. Phys. Oceanogr.*, **26**, 1881–1900, https://doi.org/10.1175/1520-0485(1996)026<1881:ANMOMP>2.0.CO;2.

——, G. S. Jaeger, M. Freilich, M. M. Omand, E. L. Shroyer, and D. Sengupta, 2016: Freshwater in the Bay of Bengal: Its fate and role in air-sea heat exchange. *Oceanography*, **29** (2), 72–81, https://doi.org/10.5670/oceanog.2016.40.

Marmorino, G. O., B. Holt, M. J. Molemaker, P. M. DiGiacomo, and M. A. Sletten, 2010: Airborne synthetic aperture radar observations of "spiral eddy" slick patterns in the Southern California Bight. *J. Geophys. Res.*, **115**, C05010, https://doi.org/10.1029/2009JC005863.

——, G. B. Smith, R. P. North, and B. Baschek, 2018: Application of airborne infrared remote sensing to the study of ocean submesoscale eddies. *Front. Mech. Eng.*, **4**, 10, https://doi.org/10.3389/fmech.2018.00010.

Maximenko, N., R. Lumpkin, and L. Centurioni, 2013: Ocean surface circulation. *International Geophysics*, Vol. 103, Elsevier, 283–304.

McWilliams, J. C., 2016: Submesoscale currents in the ocean. *Proc. Roy. Soc.*, **472**, 20160117, https://doi.org/10.1098/rspa.2016.0117.

Molinari, R., and A. D. Kirwan, 1975: Calculations of differential kinematic properties from Lagrangian observations in the western Caribbean Sea. *J. Phys. Oceanogr.*, **5**, 483–491, https://doi.org/10.1175/1520-0485(1975)005<0483:CODKPF>2.0.CO;2.

Müller, P., R.-C. Lien, and R. Williams, 1988: Estimates of potential vorticity at small scales in the ocean. *J. Phys. Oceanogr.*, **18**, 401–416, https://doi.org/10.1175/1520-0485(1988)018<0401:EOPVAS>2.0.CO;2.

Niiler, P. P., P.-M. Poulain, and L. R. Haury, 1989: Synoptic three-dimensional circulation in an onshore-flowing filament of the California Current. *Deep-Sea Res.*, **36A**, 385–405, https://doi.org/10.1016/0198-0149(89)90043-5.

——, A. S. Sybrandy, K. Bi, P. M. Poulain, and D. Bitterman, 1995: Measurements of the water-following capability of holey-sock and TRISTAR drifters. *Deep-Sea Res. I*, **42**, 1951–1964, https://doi.org/10.1016/0967-0637(95)00076-3.

Ohlmann, J. C., M. J. Molemaker, B. Baschek, B. Holt, G. Marmorino, and G. Smith, 2017: Drifter observations of submesoscale flow kinematics in the coastal ocean. *Geophys. Res. Lett.*, **44**, 330–337, https://doi.org/10.1002/2016GL071537.

Okubo, A., and C. C. Ebbesmeyer, 1976: Determination of vorticity, divergence, and deformation rates from analysis of drogue observations. *Deep-Sea Res. Oceanogr. Abstr.*, **23**, 349–352, https://doi.org/10.1016/0011-7471(76)90875-5.

Oscroft, S., A. M. Sykulski, and J. J. Early, 2020: Separating mesoscale and submesoscale flows from clustered drifter trajectories. *Fluids*, **6**, 14, https://doi.org/10.3390/fluids6010014.

Paduan, J. D., and P. P. Niiler, 1990: A Lagrangian description of motion in Northern California coastal transition filaments. *J. Geophys. Res.*, **95**, 18 095–18 109, https://doi.org/10.1029/JC095iC10p18095.

Pearson, J., B. Fox-Kemper, R. Barkan, J. Choi, A. Bracco, and J. C. McWilliams, 2019: Impacts of convergence on structure functions from surface drifters in the Gulf of Mexico. *J. Phys. Oceanogr.*, **49**, 675–690, https://doi.org/10.1175/JPO-D-18-0029.1.

Poje, A. C., and Coauthors, 2014: Submesoscale dispersion in the vicinity of the Deepwater Horizon spill. *Proc. Natl. Acad. Sci. USA*, **111**, 12 693–12 698, https://doi.org/10.1073/pnas.1402452111.

Poulain, P.-M., L. Centurioni, and T. Özgökmen, 2022: Comparing the currents measured by CARTHE, CODE and SVP drifters as a function of wind and wave conditions in the southwestern Mediterranean Sea. *Sensors*, **22**, 353, https://doi.org/10.3390/s22010353.

Ramachandran, S., and Coauthors, 2018: Submesoscale processes at shallow salinity fronts in the Bay of Bengal: Observations during the winter monsoon. *J. Phys. Oceanogr.*, **48**, 479–509, https://doi.org/10.1175/JPO-D-16-0283.1.

Redi, M. H., 1982: Oceanic isopycnal mixing by coordinate rotation. *J. Phys. Oceanogr.*, **12**, 1154–1158, https://doi.org/10.1175/1520-0485(1982)012<1154:OIMBCR>2.0.CO;2.

Righi, D. D., and P. T. Strub, 2001: The use of simulated drifters to estimate vorticity. *J. Mar. Syst.*, **29**, 125–140, https://doi.org/10.1016/S0924-7963(01)00013-6.

Rudnick, D. L., 2001: On the skewness of vorticity in the upper ocean. *Geophys. Res. Lett.*, **28**, 2045–2048, https://doi.org/10.1029/2000GL012265.

Ruiz, S., and Coauthors, 2019: Effects of oceanic mesoscale and submesoscale frontal processes on the vertical transport of phytoplankton. *J. Geophys. Res. Oceans*, **124**, 5999–6014, https://doi.org/10.1029/2019JC015034.

Saucier, W. J., 1953: Horizontal deformation in atmospheric motion. *Eos, Trans. Amer. Geophys. Union*, **34**, 709–719, https://doi.org/10.1029/TR034i005p00709.

——, 1955: *Principles of Meteorological Analysis*. University of Chicago Press, 438 pp.

Shcherbina, A. Y., E. A. D'Asaro, C. M. Lee, J. M. Klymak, M. J. Molemaker, and J. C. McWilliams, 2013: Statistics of vertical vorticity, divergence, and strain in a developed submesoscale turbulence field. *Geophys. Res. Lett.*, **40**, 4706–4711, https://doi.org/10.1002/grl.50919.

Shroyer, E., and Coauthors, 2021: Bay of Bengal intraseasonal oscillations and the 2018 monsoon onset. *Bull. Amer. Meteor. Soc.*, **102**, E1936–E1951, https://doi.org/10.1175/BAMS-D-20-0113.1.

Spydell, M. S., F. Feddersen, and J. Macmahan, 2019: The effect of drifter GPS errors on estimates of submesoscale vorticity. *J. Atmos. Oceanic Technol.*, **36**, 2101–2119, https://doi.org/10.1175/JTECH-D-19-0108.1.

Sun, D., and Coauthors, 2020: Diurnal cycling of submesoscale dynamics: Lagrangian implications in drifter observations and model simulations of the northern Gulf of Mexico. *J. Phys. Oceanogr.*, **50**, 1605–1623, https://doi.org/10.1175/JPO-D-19-0241.1.

Swenson, M. S., P. P. Niiler, K. H. Brink, and M. R. Abbott, 1992: Drifter observations of a cold filament off Point Arena, California, in July 1988. *J. Geophys. Res.*, **97**, 3593–3610, https://doi.org/10.1029/91JC02736.

Tarry, D. R., and Coauthors, 2021: Frontal convergence and vertical velocity measured by drifters in the Alboran Sea. *J. Geophys. Res. Oceans*, **126**, e2020JC016614, https://doi.org/10.1029/2020JC016614.

Thomas, L. N., A. Tandon, and A. Mahadevan, 2008: Submesoscale processes and dynamics. *Ocean Modeling in an Eddying Regime*, *Geophys. Monogr.*, Vol. 177, Amer. Geophys. Union, 17–38, https://doi.org/10.1029/177GM04.

Thushara, V., and P. N. Vinayachandran, 2014: Impact of diurnal forcing on intraseasonal sea surface temperature oscillations in the Bay of Bengal. *J. Geophys. Res. Oceans*, **119**, 8221–8241, https://doi.org/10.1002/2013JC009746.

Traon, P. Y. L., F. Nadal, and N. Ducet, 1998: An improved mapping method of multisatellite altimeter data. *J. Atmos. Oceanic Technol.*, **15**, 522–534, https://doi.org/10.1175/1520-0426(1998)015<0522:AIMMOM>2.0.CO;2.

Weller, R., and Coauthors, 2016: Air-sea interaction in the Bay of Bengal. *Oceanography*, **29** (2), 28–37, https://doi.org/10.5670/oceanog.2016.36.

Wenegrat, J. O., and M. J. McPhaden, 2016: Wind, waves, and fronts: Frictional effects in a generalized Ekman model. *J. Phys. Oceanogr.*, **46**, 371–394, https://doi.org/10.1175/JPO-D-15-0162.1.

Wijesekera, H. W., and Coauthors, 2016: ASIRI: An ocean–atmosphere initiative for Bay of Bengal. *Bull. Amer. Meteor. Soc.*, **97**, 1859–1884, https://doi.org/10.1175/BAMS-D-14-00197.1.